

Chapter 28

Influence of Filter Structure and Casting System on Filtration Efficiency in Aluminum Mold Casting



Benedict Baumann, Andreas Keßler, Claudia Dommaschk, and Gotthard Wolf

28.1 Introduction

In 1974, the company Swiss Aluminium Limited developed the first ceramic foam filters for the filtration of liquid metal to increase the purity of the molten metal [1]. Only one year later, another patent was registered, which improved the ceramic foam filter concerning its properties [2]. Since then, ceramic foam filters have been continuously improved as well as modified and are now available on the market in a variety of different materials, porosities, sizes, and geometries. In the cause of the energy-intensive raw aluminum production, the use of secondary raw materials becomes more and more important. Through this the melts get more contaminated with impurities; the further development of foam ceramic filters is essential for the foundry industry. Through this, the SFB 920 started with the development of intelligent filter materials and filter systems. The SFB 920 is focusing on the further development of filter materials for ceramic foam filters for the foundry industry. Thus, a major contribution to Zero Defect Materials has already been made for molten metal filtration.

B. Baumann (✉) · A. Keßler · C. Dommaschk · G. Wolf
Foundry Institute, Technische Universität Bergakademie Freiberg, Bernhard-von-Cotta-Str. 4,
09599 Freiberg, Germany
e-mail: Benedict.Baumann@gi.tu-freiberg.de

A. Keßler
e-mail: Andreas.Kessler@gi.tu-freiberg.de

C. Dommaschk
e-mail: Claudia.Dommaschk@gi.tu-freiberg.de

G. Wolf
e-mail: Gotthard.Wolf@gi.tu-freiberg.de

In foundry practice, those high-performance filters are used for the separation of exo- and endogenous non-metallic impurities that reduce the mechanical and casting properties of parts. In addition to cleaning the melt, the filters also ensure laminar flow in the gating system and thus prevent new oxide formation in the mold cavity. Thus, filters in the casting system offer the possibility of sustainably cleaning the melt during the casting process, i.e. directly before the mold is filled. The implementation of the ceramic foam filter in the gating system does not follow any clear rules and in foundry practice is usually guided by the available space on the pattern plate and, in the best case, by the design recommendations of the filter manufacturer. In conventional foundry simulations, the filter is only considered as a flow resistance for the melt. A prediction of the filtration effect is hardly possible with the simulation programs. Simulations have also been used in foundry research mainly to study the flow behavior of the melt through the filter. For example, Barkhudarov and Hirt [3] simulated the formation of impurities as a result of turbulent mold filling. Zadeh and Campbell [4] compared simulation results from MagmaSoft and Flow-3D with results from real casting trials. They could not find any correlation between the results, because the simulations do not take into account the formation of oxide surfaces on the melt front and the cooling of the melt through the filter. A more microscopic approach was taken by Acosta et al. [5–7] and Werzner et al. [8, 9] by simulating the flow of the melt in the separate pores and examined the effect of the flow on the deposition of the impurities on the pore walls. The simulations were limited to separate pores only and not to the total filter system. Thus, the effect of the filter position in the casting system on the filtration efficiency of the ceramic foam filters has not yet been adequately investigated on a macroscopic level.

The present work investigates the effect of filter position on the filtration efficiency of ceramic foam filters. For this purpose, real filter structures are scanned by micro-computed tomography. This scan is then loaded as an STL file into the simulation program Flow-3D. Thus, it is possible to investigate the four most common filter positions concerning their filtration efficiency. Furthermore, it is investigated how far the length of the filter and the roughness of the filter surface influence the particle filtration. The simulation results are then compared with results from real casting trials.

28.2 Simulation

The CFD simulation program Flow-3D from Flow Science is used for the simulations. The program is able to represent the filter as an independent structure in the casting system as well as the implementation of particles in a defined number and size. In the following, the further parameters of the simulations will be explained in more detail.

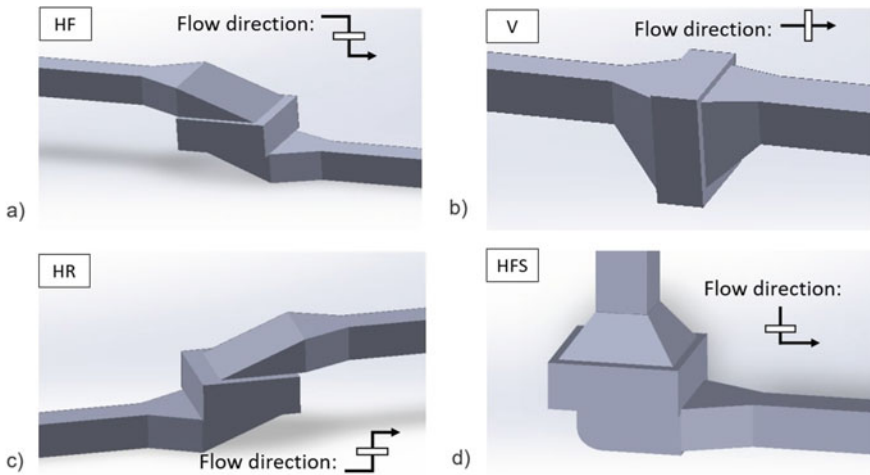


Fig. 28.1 Examined filter positions **a** horizontally falling (HF); **b** vertically (V); **c** horizontally rising (HR); **d** horizontally falling sprue (HFS) [11]

28.2.1 Geometry

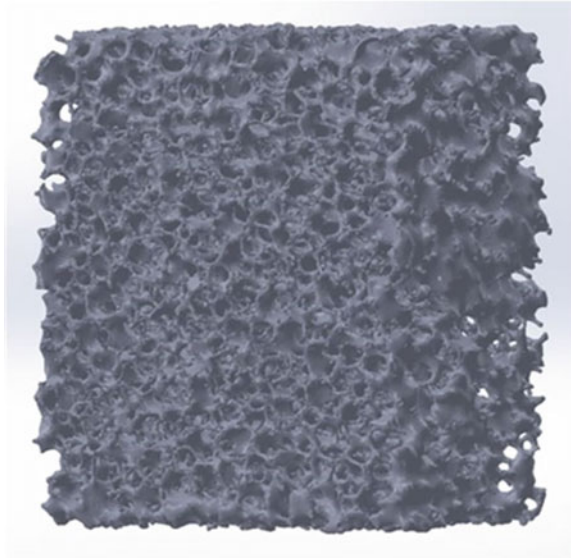
For the simulations, four different filter chamber geometries respectively filter positions are investigated which can be seen in Fig. 28.1. The design of the filter chamber geometry was based on the design guidelines of Campbell [10]. Campbell set up the guidelines about a maximum possible laminarization of the melt as well as concerning foundry-specific framework conditions, but not with the focus on achieving the highest possible separation efficiency. The simulated filter chamber geometries are thus also used in practice and can be described as follows:

- (a) Filter position HF: The filter lies **h**orizontally in the runner and is flowed through from top to bottom (**f**alling).
- (b) Filter position V: The filter stands **v**ertically in the runner.
- (c) Filter position HR: The filter lies **h**orizontally in the runner and is flowed through from bottom to top (**r**ising).
- (d) Filter position HFS: The filter is located **h**orizontally below the sprue and the flow is from top to bottom (**f**alling).

28.2.2 Filter

Real filter geometries are used for the simulations with Flow-3D. To generate the filter geometries, commercially available 20 and 30 ppi ceramic foam filters with dimensions of $50 \times 50 \times 22$ mm are scanned using micro-CT. The scanned data set is then converted into an STL file (see Fig. 28.2) and can be used directly in

Fig. 28.2 Data set of a ceramic foam filter geometry scanned by micro-CT and converted into an STL file [11]



Flow-3D as geometry. To define the geometry as a filter in the simulation, the filter is defined with certain parameters. These parameters are the surface roughness of the filter and the drag coefficient. The drag coefficient defines how well or poorly the particles adhere to the filter when they come into contact with it. For the simulations, the drag coefficient is defined with the parameter 1, which means that every particle that touches the filter sticks to the filter wall and is thus separated from the melt. The surface roughness is used to define the filter material. For aluminum casting alloys, filters made of alumina are used in practice. Fankhänel et al. [12] measured the roughness of various filter materials and found, among other results, that the surface roughness of alumina filters is $1.7 \mu\text{m}$. For the simulations, the surface roughness is thus defined as $1.7 \mu\text{m}$. Furthermore, a simulation series is carried out with a surface roughness of $7.3 \mu\text{m}$. This value corresponds to the surface roughness of mullite filters and represents a high contrast to the surface roughness of the alumina filters to investigate a possible influence of the roughness of the filters on the separation efficiency. To investigate the possible influence of the length of the filter on the filtration efficiency, the filter position HF is also simulated with a double-length 30 ppi filter in the dimensions $50 \times 50 \times 44 \text{ mm}$ and surface roughness of $1.7 \mu\text{m}$. The STL file of the 30 ppi filter is multiplied and arranged in series so that the two filters are connected in a row and thus produce a longer filter.

28.2.3 Melt

An AlSi7Mg0.3 is selected as the aluminum casting alloy for the simulation. To minimize the computation time for the simulations, heat transfer processes between melt and mold wall as well as melt and filter are not considered.

28.2.4 Particle

Voigt et al. [13] and Le Brun et al. [14] investigated the separation efficiency of ceramic foam filters for continuous aluminum casting in practical casting tests at Constellium. A defined impurity content was set in the melt and the number, as well as size of the particles before and after the filter, were measured using LiMCA. Powdered alumina (Al_2O_3) and powdered spinel (MgAl_2O_4) were added to the melt to ensure a high impurity content in the melt. From over 140 individual measurements, an average particle count of 17,500 particles was determined, which is also the number of particles that flow through the filter per simulation. It should be noted that this is the number of particles in an intended contaminated melt. The impurity content does not represent the impurity content in industrial foundry practice. Table 28.1 shows the two particle types used in the simulation with their density, size, and number.

As with the tests at Constellium, two different types of particles are defined for the simulation to investigate the deposition efficiency of different types of particles. On the one hand, the deposition of aluminum oxide is analyzed, cause it is the most frequently occurring non-metallic inclusion in aluminum melts, and on the other hand, the deposition of spinel particles are examined, which can form in aluminum melts due to the production process. The spinel particles were intentionally chosen to be larger because they can grow in the melt and are therefore larger than the usually finely distributed oxide skins. Apart from the density, size, and distribution of the particles, no other parameters such as the shape or surface properties of the particles can be defined. Furthermore, there are no interactions between the particles themselves, and between particles and mold walls as well as particles and melt.

Table 28.1 Overview of the particles used in the simulations [11]

Type	Density [g/cm^3]	Size [μm]	Percentage [%]	Quantity [number]
Al_2O_3 (Alumina)	3.95	25	45	7875
		35	30	5250
		45	7.5	1313
MgAl_2O_4 (Spinel)	3.5	45	7.5	1312
		55	5	875
		80	5	875

Since the particles are much smaller than the pore diameter of the filters and there are no interactions between the individual particles, only deep-bed filtration can be represented with the simulation, but not cake or sieve filtration.

28.2.5 Further Boundary Conditions

Figure 28.3 shows the simulation process using the example of the HF filter layer with a 20 ppi filter. As can be seen, the particles are arranged in a bulk in front of the filter. To reduce the computing time of the simulations, the system is described as semi-stationary, i.e. at the beginning of the simulation the mold cavity is already filled with melt. The driving force for the melt flow is the metallostatic pressure respectively the geometry of the sprue. The metallostatic pressure can be regarded as approximately the same for all filter positions. When the melt is set in motion at the start of the simulation, the particles are also carried along by the melt flow and thus pass through the filter. The simulation runtime is limited to the duration of the filtration process. The simulation is completed when all free particles not bound in the filter have left the filter. To reduce the computing time even further, the entire filter is not examined, but only a 10 mm thick section, so that the examined area has a size of $50 \times 10 \times 22$ mm.

To investigate in which areas of the filter particles were deposited, the filters are subdivided into 3 segments for evaluation. Figure 28.4 shows an example of the subsections for the filter layer HF and V.

Table 28.2 shows all 13 simulations performed with the respective parameters, where the number and type of particles are always identical.

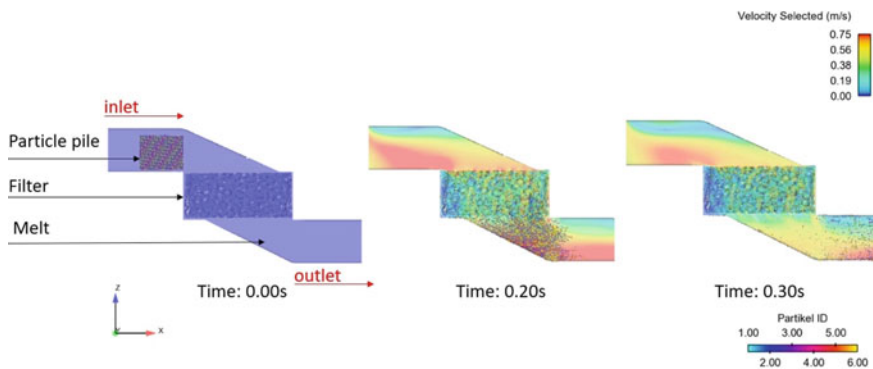


Fig. 28.3 Example of a simulation with the filter position HF for a 20 ppi filter [11]

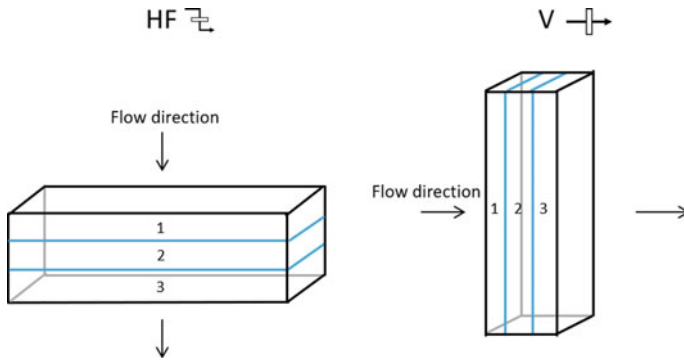


Fig. 28.4 Subdivision of the filters into individual segments

Table 28.2 Summary of all simulations performed with the different variables

Simulation number	Variables			
	Position filter chamber	Filter length [mm]	Filter porosity [ppi]	Surface roughness (μm)
1	HF	22	20	1,7
2	HF	22	30	1,7
3	V	22	20	1,7
4	V	22	30	1,7
5	HR	22	20	1,7
6	HR	22	30	1,7
7	HFS	22	20	1,7
8	HFS	22	30	1,7
9	HF	22	20	7,3
10	HF	22	30	7,3
11	V	22	20	7,3
12	V	22	30	7,3
13	HF	44	30	1,7

28.3 Results of the Simulation

To compare the different filter positions, the filtrations efficiency E was calculated for each one. The filtration efficiency E is defined through the number of particles before or in the filter and the number of particles after the filter. Where N_0 stands for the number of particles before or in the filter and N_1 for the number of particles after the filter.

$$E = \left(1 - \frac{N_0 - N_1}{N_0} \right) \times 100[\%] \tag{28.1}$$

Table 28.3 Filtration efficiencies determined in the simulations [11]


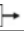


Filter position	20 ppi efficiency (%)	30 ppi efficiency (%)	Percentage increase (%)
HF 	27.9	36.8	31.9
V 	22.7	33.2	46.3
HR 	23.4	29.5	26.1
HFS 	20.8	33.2	59.6

Table 28.3 gives an overview of the filtration efficiencies of the individual filter positions for the simulation of the 20 and 30 ppi filters with a surface roughness of 1.7 μm . As can be seen, the filter position in which the filter lies horizontally in the runner and is flowed through from top to bottom (HF) has the highest filtration efficiency for both types of filters 20 and 30 ppi. For all filter positions, a clear increase in filtration efficiency of at least 26% can be observed when using a 30 ppi filter compared to a 20 ppi filter. Especially for the filter positions where the melt flows directly into the filter (V and HFS), a significant increase in filtration efficiency of at least 46% can be observed.

28.3.1 Influence of Particle Size on Filtration Efficiency

To determine a possible influence of the simulated particle sizes (see Table 28.1) on the separation performance, the filtration efficiency of the individual particle sizes was determined for each filter position. The results for the 20 and 30 ppi filters are shown in Figs. 28.5 and 28.6. It can be also seen that the HF filter position has the highest filtration efficiency across all particle size classes for the 20 and 30 ppi filters. For the 20 ppi filters, there is generally no concrete difference in the filtration efficiency of the individual particle sizes from 25 to 80 μm . Even with the 30 ppi filters, there is hardly any significant difference between the particle sizes of 25 μm up to 55 μm . Only from a particle size of 80 μm is an increase in filtration efficiency noticeable. The differences between the individual particle size classes are too small compared to the pore diameter of the filter and so no significant difference can be proved. It is expected that the filtration efficiency increases with increasing particle size or decreasing pore size.

28.3.2 Influence of Particle Type on Filtration Efficiency

The particle size of 45 μm was used to study the influence of the particle type on the filtration efficiency. The same number of alumina particles and spinel particles were defined for each simulation (see Table 28.1). Table 28.4 shows the filtration efficiencies of the 45 μm particles at the HF and HFS filter positions for the 20

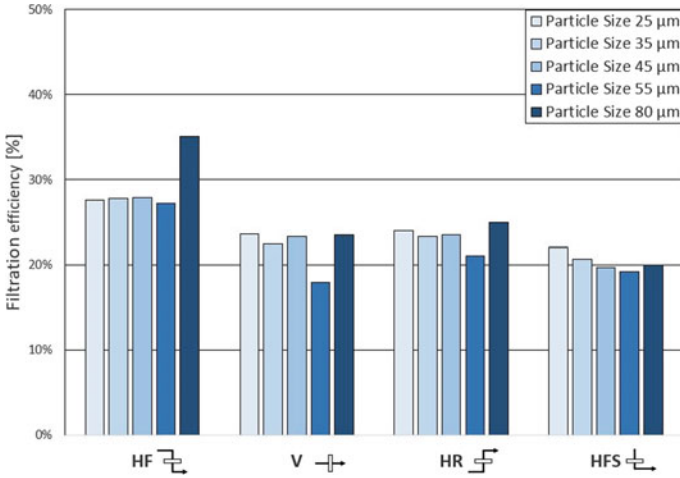


Fig. 28.5 Filtration efficiency of the different filter positions for the various particle sizes for the simulations with a 20 ppi filter [11]

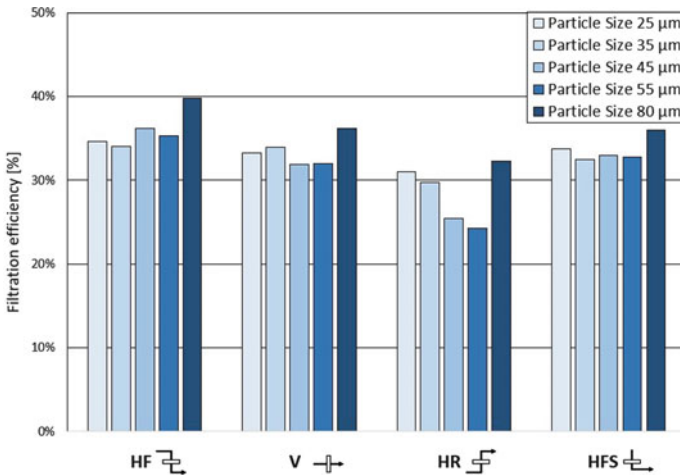






Fig. 28.6 Filtration efficiency of the different filter positions for the various particle sizes for the simulations with a 30 ppi filter [11]

and 30 ppi filters, respectively. As can be seen, the filtration efficiencies do not differ significantly. The largest change is for the HF filter position (30 ppi) with a difference of 3.4% points. The two different particle types were separated with an average difference of approximately 1% point. Thus, the influence of the particle type in the simulation is negligible. Probably the difference in density between the two particles is too small to cause a difference in filtration efficiency.

Table 28.4 Filtration efficiencies of the 45 μm alumina and spinel particles [11]

Filter position	Filter porosity [ppi]	Alumina particles 45 μm	Spinel particles 45 μm
		Filtration efficiency [%]	Filtration efficiency [%]
HF 	20	27.9	27.7
HF 	30	37.9	34.5
HFS 	20	19.8	19.4
HFS 	30	32.8	32.9

28.3.3 Deposition of Particles in the Filter

To investigate where the particles are deposited in the filter, the simulated filters were divided into 3 segments as shown in Fig. 28.4. Table 28.5 shows the respective proportion of particles deposited in one of the three areas for the filter positions HF and V for 20 and 30 ppi filters respectively.

As can be seen from the table, the difference between 20 and 30 ppi filters at filter position HF is between 0.1 and 0.4% points. For filter position V, the distinctions are also only 0.6 to 1.8% points, so no significant difference can be detected between 20 and 30 ppi filters. However, it can be seen from the table that the particles in filter position HF are deposited mainly in the first third of the filter (approx. 44%) and that the sedimentation of the particles decreases with increasing filter length. In comparison, the particles in filter layer V are deposited to a likewise high degree in all 3 segments. One possible reason for this could be found in the flow direction of the filters. Whereas with filter layer HF the melt has to be redirected before it passes the filter, with filter layer V the melt flows directly through it. The redirection slows down the melt, which leads to better filtration efficiency [15] and thus explains the increased separation efficiency.

Table 28.5 Percentage of deposited particles in each filter plane, as well as the difference (Δ) between 20 and 30 ppi [11]



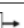
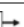




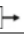
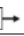
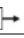
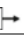
		Filter plane					
Filter position	Filter porosity [ppi]	1		2		3	
		Fraction of filtered particles [%]	Δ	Fraction of filtered particles [%]	Δ	Fraction of filtered particles [%]	Δ
HF 	20	44.2	0.4	31.4	0.1	24.4	0.3
HF 	30	43.8		31.5		24.7	
V 	20	35.0	0.6	36.0	1.8	29.0	1.3
V 	30	35.6		34.2		30.2	

Table 28.6 Comparison of filtration efficiency with a different surface roughness of the filters

Filter			Filtration efficiency [%]	
Position	Surface roughness [μm]	Filter porosity [ppi]	Total	Δ
HF 	1,7	20	27,9	-3,1
HF 	7,3	20	24,8	
HF 	1,7	30	36,8	-2,5
HF 	7,3	30	34,3	
V 	1,7	20	22,7	-1,4
V 	7,3	20	21,3	
V 	1,7	30	33,2	-0,7
V 	7,3	30	32,5	

28.3.4 Influence of the Surface Roughness of the Filter on the Filtration Efficiency

To investigate a possible influence of the surface roughness of the filter on the filtration efficiency, the filter positions HF and V were simulated with a surface roughness of 1.7 μm on the one hand and with a surface roughness of 7.3 μm on the other hand for 20 and 30 ppi filters (see Table 28.2). The calculated filtration efficiencies are shown in Table 28.6.

As can be seen from the table, the filtration efficiencies are always lower for the filters with higher surface roughness. It should be noted that the difference in filtration efficiency for filter position HF, with a max. of 3.1% points, is significantly higher than for filter position V, which has a difference of 1.4% points. Since, due to the redirection, the melt flows through the filter more slowly at filter position HF than at filter position V, it is therefore possible that the surface roughness of the filter has a more significant effect on the filtration efficiency at slower flow rates than at faster flow rates.

28.3.5 Influence of Filter Length on Filtration Efficiency

To investigate the influence of the filter length on the filtration efficiency, a 30 ppi filter with a double filter length of 44 mm was simulated at a surface roughness of 1.7 μm for the filter layer HF. Table 28.7 shows the results of the simulation using the double filter length as well as the single filter length with otherwise identical parameters.

As can be seen, the difference between the two filtration efficiencies is 13.7% points, which corresponds to an increase of approx. 37%. Therefore, a filter twice as long is much more efficient in filtering particles. In this simulation, the filter is again

Table 28.7 Comparison of filtration efficiencies with different filter lengths





Filter			Filtration efficiency [%]	
Position	Filter length [mm]	Filter porosity [ppi]	Total	Δ
HF 	22	30	36,8	+13,7
HF 	44	30	50,5	

Table 28.8 Percentage of deposited particles in each filter plane, as well as the difference between 22 and 44 mm filter length

Filter position	Filter length [mm]	Filter plane		
		1	2	3
		Fraction of filtered particles [%]	Fraction of filtered particles [%]	Fraction of filtered particles [%]
HF 	22	43,8	31,5	24,7
HF 	44	47,0	30,1	22,8



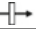
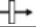


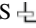
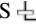


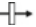
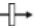

divided into 3 segments to investigate in which areas the particles are deposited in the filter (see Table 28.8).

Just as with the normal filter length of 22 mm, almost half of the particles are located in the first third of the filter when using a filter length of 44 mm.

28.4 Summary of the Simulations

Table 28.9 shows all simulations with the variables: Filter position, filter length, porosity, and surface roughness of the filter as well as the corresponding filtration efficiencies. For each filter position, the use of a 30 ppi filter increases the filtration efficiency by 26% up to 59.6% which corresponds to an average increase of about 42.4% compared to a 20 ppi filter. The filter position HF has the highest filtration efficiency for both the 20 ppi and 30 ppi filters. Increasing the surface roughness of the filters from 1.7 to 7.3 μm leads to a marginal reduction in filtration efficiency, and the filter position HF achieves a higher filtration efficiency than the filter position V again. By doubling the filter length from 22 to 44 mm, the filtration efficiency of the filter position HF was increased by 37% to 50.5%, which provides the highest filtration efficiency. It should be noted, however, that most particles are deposited in the first third of the filter and that in practice a longer filter can lead to increased cooling of the melt and thus to freezing of the melt in the filter.

Table 28.9 Summary of all simulations with the corresponding variables as well as the filtrate efficiencies

Simulation number	Variables				Filtration efficiency [%]
	Filter position	Filter length [mm]	Filter porosity [ppi]	Surface roughness (μm)	
1	HF 	22	20	1,7	27,9
2	HF 	22	30	1,7	36,8
3	V 	22	20	1,7	22,7
4	V 	22	30	1,7	33,2
5	HR 	22	20	1,7	23,4
6	HR 	22	30	1,7	29,5
7	HFS 	22	20	1,7	20,8
8	HFS 	22	30	1,7	33,2
9	HF 	22	20	7,3	24,8
10	HF 	22	30	7,3	34,3
11	V 	22	20	7,3	21,3
12	V 	22	30	7,3	32,5
13	HF 	44	30	1,7	50,5

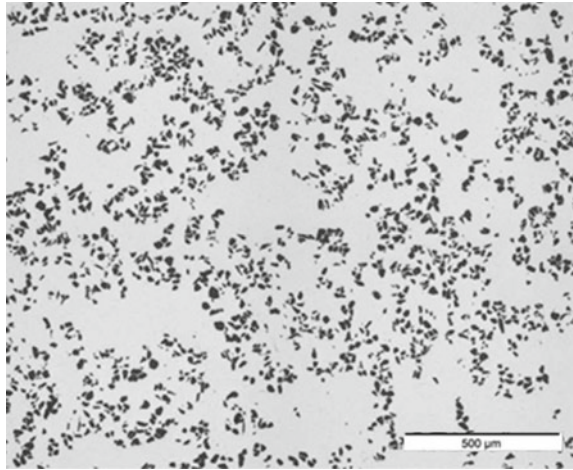
28.5 Casting Trials

The simulations have shown that the deposition of particles in the filter depends on the filter position. To verify this, casting trials are carried out by adding foreign particles to a melt and then casting it in four molds with the filter positions used in the simulations. The castings were generated with both 20 and 30 ppi filters. The casting trials aim to analyze the deposition behaviors of the particles in the filter. Since in reality deep-bed filtration, as well as sieve and cake filtration, are effective, a comparison of the filtration efficiency between simulation and casting trials is not useful.

28.5.1 Geometry

As in the simulations, the filter positions HF, V, HR, and HFS (see Fig. 28.1) are also examined in the casting trials. The corresponding models differ only in the design of the filter chamber and are otherwise identical from the casting technology point of view. The main focus of the models is that design-related influencing factors are minimized and the results can only be assigned to the different filter chamber geometries. The molds are all made of furan resin-bonded molding material.

Fig. 28.7 Micrograph of the Duralcan® alloy with 15 wt% Al₂O₃



28.5.2 Filter

For the casting trials, only filters made of alumina with dimensions of 50 × 50 × 22 mm from Hofmann Ceramic GmbH (Breitscheid, Germany) with porosities of 20 ppi and 30 ppi were used. The filters from Hofmann Ceramic GmbH were also used for the micro-CT scan and thus for the simulations.

28.5.3 Melt with Foreign Particles

As in the simulations, an AlSi7Mg0.3 is used as the base alloy for the casting trials. To investigate the behavior of the particles during the filtration process, Duralcan® is added to the melt. Duralcan® is a metal matrix composite (MMC) that is normally used for “high-end” applications such as the frame of the space shuttle [16]. Duralcan® consists of an aluminum matrix reinforced with Al₂O₃ particles. To enrich the melt with 20 μm of foreign particles, Duraclan® was added. Figure 28.7 shows a micrograph of the Duralcan® master alloy used, which is reinforced with 15% Al₂O₃ particles.

28.5.4 Execution of the Casting Trials

The melt is prepared in a resistance-heated 20 kW crucible furnace with a capacity of 30 kg of molten aluminum. Per batch, 27 kg of ingot material of the alloy AlSi7Mg0.3 is melted and degassed for 20 min with an impeller. At a temperature of 750 °C, 3 wt.% Duralcan® is added, which corresponds to 0.8 kg Duralcan® on the total melting

quantity. Before the metal is transferred from the crucible to the ladle, it is homogenized manually by stirring with a graphite rod. This ensures that the Al_2O_3 particles are homogeneously distributed in the melt and their sedimentation is prevented. The alloy was poured with a casting temperature of 730 °C. From one crucible, 8 molds with the same filter chamber geometry are cast. After solidification and cooling of the metal, the casting is removed from the mold and the filter chamber with the filter cast in it is prepared for metallographic examinations.

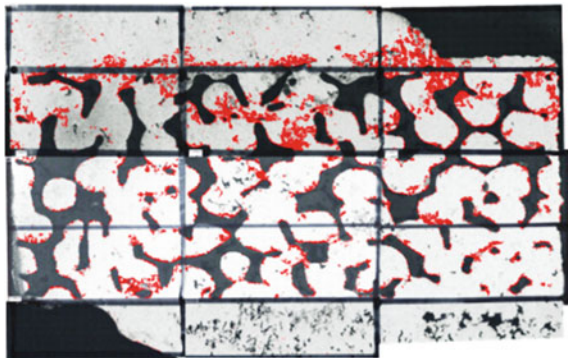
28.5.5 Metallographic Examinations of the Filter

Like the simulations, the filters are also divided into three segments (see Fig. 28.4). Individual images of each zone are made by using a 3D microscope with $200 \times$ magnification. This was fitted into a panoramic image and processed by image analysis. The size, morphology, and appearance of the particles are known from previous investigations and therefore a simple identification of the particles is enabled. Figure 28.8 shows an example of the metallographic evaluation of a 20 ppi filter with the filter position HF. The red-colored areas are the filtered Al_2O_3 particles from the Duralcan® alloy.

28.6 Results of the Casting Trials

As in the simulations, the filters were also divided into 3 sections for the casting trials (see Fig. 28.4) to investigate where the particles were deposited in the filter. Figure 28.9 shows the assembled photomicrographs of the filter positions examined for the 20 and 30 ppi filters and the percentage of particles deposited in each plane. The color scale helps to identify especially effective zones. As can be seen in the figure, in all filter positions where the flow is vertical (HFS, HF, HR), approx. 50

Fig. 28.8 Example of filter evaluation using filter position HF with a 20 ppi filter [11]



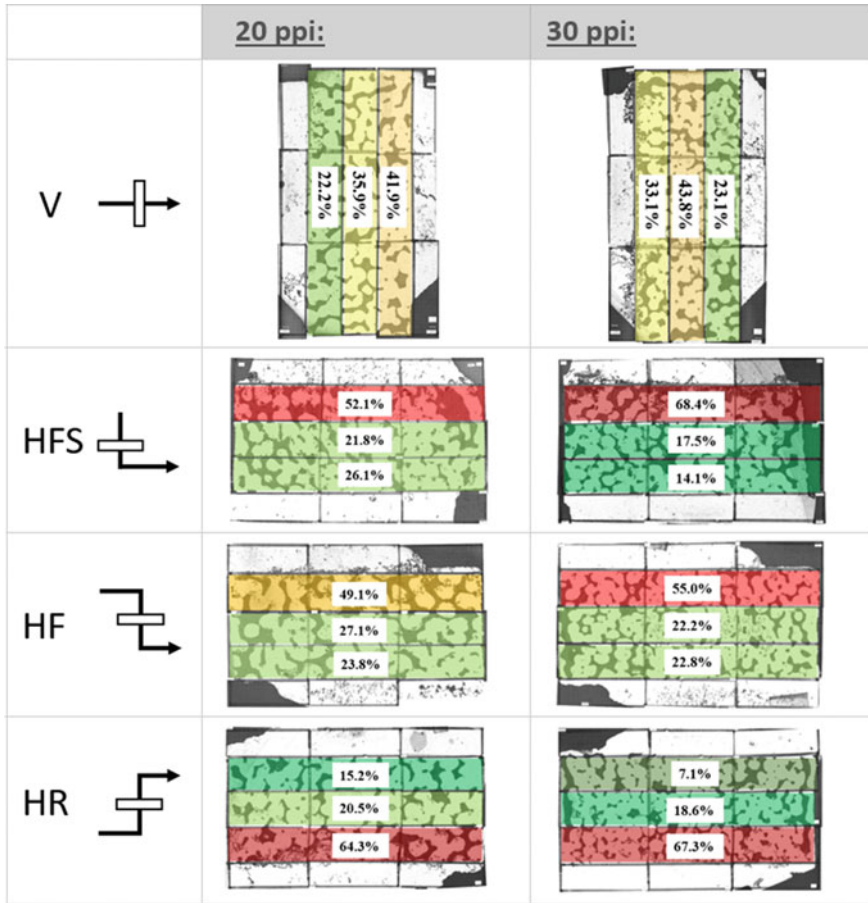


Fig. 28.9 Percentage of deposited particles in each filter plane for the cast filter positions V, HFS, HF, and HR for the 20 and 30 ppi filters

to almost 70% of all particles are separated in the first third of the filter. In almost all cases, the filtration effect decreases with increasing filter length, so that in the last third of the filter only 7 to 26% of the particles are separated. The deposition of particles behaves differently in filter position V, where the filter stands horizontally in the mold. In this filter position, the deposition of particles in the individual filter levels is more uniform and ranges between 22 and 44%. This could be due to the increased flow rate compared to the other filter positions, which ensures that the particles are carried further into the depth of the filter. In the filter position HFS, the filtration efficiency is at its highest in the first third of the filter, despite the increased melt velocity. This can be due to the fact that, in this filter position, the melt hits the filter directly from the gate and is therefore strongly turbulent, which leads to the formation of oxides. These oxides are separated by sieve and cake filtration upstream

of the filter so that the 20 μm Al_2O_3 particles are separated primarily by the effect of cake filtration in the first third of the filter. It was also observed in the simulations that the particles are deposited more uniformly over the total filter length in filter position V and that most of the particles are deposited in the first third of the filter in filter position HF.

28.7 Conclusion

In the present work, the influence of the filter position on the filtration efficiency of 20 ppi and 30 ppi ceramic foam filters was investigated for the first time by means of numerical simulations. Part of the simulation results was subsequently evaluated with real casting trials. Both the simulations and the casting trials were able to show similar separation behavior of the particles in the filter layers. This demonstrates that the numerical simulation of particle filtration from a metallic melt gives predictions in reasonable agreement with experimental measurements.

The following conclusions are drawn from the simulations:

- The highest filtration efficiency is achieved when the filter is placed horizontally in the runner and the flow is from top to bottom.
- In all filter positions where the filter lies horizontally in the runner, deposition of inclusions occurs primarily in the first third of the filter. If the filter is positioned vertically in the runner, deposition tends to occur more uniformly along the length of the filter. This could also be proven with real casting trials.
- The simulations have shown that the roughness of the filter surface has a minor influence on the filtration efficiency. The filtration efficiency decreases slightly when the roughness of the filter surface increases.
- By doubling the filter length from 22 to 44 mm, a 37% increase in filtration efficiency can be achieved for Al_2O_3 particles with a size of 20 μm . Nevertheless, 47% of the particles are deposited in the first 15 mm of the 44 mm long filter, so that the use of longer filters is not advised from a foundry technology point of view [17].

Acknowledgements The authors would like to acknowledge the German Research Foundation (Deutsche Forschungsgemeinschaft, DFG) for funding this work and project as a part of the Collaborative Research Centre 920 “Multi-Functional Filters for Metal Melt Filtration – A Contribution towards Zero Defect Materials” (Project ID: 169148856 – CRC 920, Subproject S03).

Particular acknowledgment is expressed to the commitment of the staff members of the Foundry Department, especially to Mr. Klaus Eigenfeld, Mrs. Eva Hoppach, and Mr. Björn G. Dietrich.

References

1. J.P. Michael, T.J. Gray, U.S. Patent 3,893,917, 8 July 1975
2. J.C. Yarwood, J.E. Dore, R.K. Preuss, U.S. Patent 3,962,081, 8 June 1976
3. M.R. Barkhudarov, C.W. Hirt, Tracking defects. (Flow Science, Inc.) <https://www.flow3d.com/wp-content/uploads/2014/08/Tracking-Defects.pdf>. Accessed 03 June 2022
4. A. Zadeh, J. Campbell, AFS transactions. 02–020 (2002)
5. F.A. Acosta G., A.H. Castillejos E., Metall. Mater. Trans. B **31**, 491–502 (2000). <https://doi.org/10.1007/s11663-000-0155-3>
6. F.A. Acosta G., A.H. Castillejos E., Metall. Mater. Trans. B **31**, 503–514 (2000). <https://doi.org/10.1007/s11663-000-0156-2>
7. F.A. Acosta G., A.H. Castillejos E., J.M. Almanza R., A. Flores V., Metall. Mater. Trans. B **26**, 159–171 (1995). <https://doi.org/10.1007/BF02648988>
8. C. Demuth, E. Werzner, M.A.A. Mendes, H. Krause, D. Trimis, S. Ray, Adv. Eng. Mater. **19** 9, (2017). <https://doi.org/10.1002/adem.201700238>
9. E. Werzner, M. Abendroth, C. Demuth, C. Settgest, D. Trimis, H. Krause, S. Ray, Adv. Eng. Mater. **19** 9, (2017). <https://doi.org/10.1002/adem.201700240>
10. J. Campbell (ed.), *Complete Casting Handbook. Metal Casting Processes, Metallurgy, Techniques and Design*, (Butterworth-Heinemann Ltd, Oxford, 2015)
11. B. Baumann, A. Kessler, E. Hoppach, G. Wolf, M. Szucki, O. Hilger, Arch. Foundry Eng. Vo. **21**(3), 70–80 (2021). <https://doi.org/10.24425/afe.2021.138668>
12. B. Fankhänel, M. Stelter, C. Voigt, C.G. Aneziris, Adv. Eng. Mater. **19** 9, (2017). <https://doi.org/10.1002/adem.201700084>
13. C. Voigt, E. Jäckel, F. Taina, T. Zienert, A. Salomon, G. Wolf, C.G. Aneziris, P. Le Brun, Metall. Mater. Trans. B. **48**(1), 497–505 (2017). <https://doi.org/10.1007/s11663-016-0869-5>
14. P. Le Brun, F. Taina, C. Voigt, E. Jäckel, C.G. Aneziris, in E. Williams (Eds.), *Light Metals* 785–789 (2016). https://doi.org/10.1007/978-3-319-48251-4_133
15. H. Duval, C. Rivière, É. Laé, P. Le Brun, J. Guillot, Metall. Mater. Trans. B. **40**(2), 233–246 (2009). <https://doi.org/10.1007/s11663-008-9222-y>
16. O. Beffort, Metal matrix composites: properties, applications and machining (in German), Paper presented at the 6. Internationales IWF-Kolloquium, ETH Zürich, Egerkingen, Schweiz, 18–19 April 2002
17. E. Jäckel, Dissertation. Technische Universität Bergakademie Freiberg (2019)

Open Access This chapter is licensed under the terms of the Creative Commons Attribution 4.0 International License (<http://creativecommons.org/licenses/by/4.0/>), which permits use, sharing, adaptation, distribution and reproduction in any medium or format, as long as you give appropriate credit to the original author(s) and the source, provide a link to the Creative Commons license and indicate if changes were made.

The images or other third party material in this chapter are included in the chapter's Creative Commons license, unless indicated otherwise in a credit line to the material. If material is not included in the chapter's Creative Commons license and your intended use is not permitted by statutory regulation or exceeds the permitted use, you will need to obtain permission directly from the copyright holder.

